A Material Perspective on HgTe Nanocrystal-based Short Wave Infrared Focal Plane Arrays

Huichen Zhang, Rodolphe Alchaar, Yoann Prado, Adrien Khalili, Charlie Gréboval, Mariarosa Cavallo, Erwan Bossavit, Corentin Dabard, Tung Huu Dang, Claire Abadie, et al.

A Material Perspective on HgTe Nanocrystal-based Short Wave Infrared Focal Plane Arrays

Huichen Zhang[1$], Rodolphe Alchaar[1$], Yoann Prado[1], Adrien Khalili[1], Charlie Gréboval[1], Mariarosa Cavallo[1], Erwan Bossavit[1], Corentin Dabard[2], Tung Huu Dang[1], Claire Abadie[1], Christophe Methivier[3], David Darson[4], Victor Parahyba[5], Pierre Potet[5], Julien Ramade[6], Mathieu G. Silly[7], James K. Utterback[1], Debora Pierucci[1], Sandrine Ithurria[2], Emmanuel Lhuillier[1*]

[1] Sorbonne Université, CNRS, Institut des NanoSciences de Paris, INSP, 75005 Paris, France.
[2] Laboratoire de Physique et d'Etude des Matériaux, ESPCI-Paris, PSL Research University, Sorbonne Université Univ Paris 06, CNRS UMR 8213, 10 rue Vauquelin 75005 Paris, France.
[3]Laboratoire de Réactivité de Surface, UMR CNRS 7197, Sorbonne Universités, 4 place Jussieu, 75005 Paris, France
[4] Laboratoire de Physique de l'École normale supérieure, ENS, Université PSL, CNRS, Sorbonne Université, Université Paris Cité, Sorbonne Paris Cité, 75005 Paris, France.
[5] New Imaging Technologies SA, 1 impasse de la Noisette 91370 Verrières le Buisson, France.
[6]Institut Pprime, Département Physique et Mécanique des Matériaux, UPR 3346 CNRS, Université de Poitiers, SP2MI, TSA 41123, 86073 Poitiers Cedex 9, France
[7]Synchrotron-SOLEIL, Saint-Aubin, BP48, 91192 Gif sur Yvette Cedex, France.

Abstract: After the use of nanocrystals as light down-converters, infrared sensing appears to be one of the first market applications where they can be used while being both electrically and optically active. Over recent years, tremendous progress has been achieved, leading to an apparent rise in the technological readiness level (TRL). So far, the efforts have been focused on PbS nanocrystals for operation in the near-infrared. Here, we focus on HgTe since its narrower band gap offers more flexibility to explore the extended short-wave and mid-wave infrared. We report a photoconductive strategy fort the design of short wave infrared focal plane array with enhanced image quality. An important aspect often swept under the rug at an early stage is the material stability. It appears that HgTe remains mostly unaffected by oxidation under air operation. The evaporation of Hg, a potentially dramatic aging process, only occurs at temperatures far beyond the focal plane array's standard working temperature. The main bottleneck appears to be the particle sintering resulting from joule heating of focal plane array. This suggests that a cooling system is required, with a first role of preventing the material from sintering even before targeting dark current reduction.

[$] these authors have equal contributions

*To whom correspondence should be sent: el@insp.upmc.fr

Introduction

Nanocrystals (NCs) have become viable building blocks for optoelectronics. Quantum confinement enables a straightforward tunability of their spectral properties. As a zero band gap semiconductor, HgTe[1–6] offers a particularly broad tunability in the infrared with optical features varying from the visible to the THz range[7]. This has enabled the integration of HgTe as an optically active material in an extensive range of devices such as LEDs,[8–10] lasers[11–13], photonic structures[14–16], infrared sensors[17–24], and cameras[25]. Following their use as light down-converters in displays and farming, nanocrystals are now being integrated into infrared cameras[25–28], one of the first commercial applications in which the material is both electrically and optically active. So far, most reported cameras[29,30] are based on PbS nanocrystals and operate in the near and short-wave infrared[26–28,31–33]. HgTe holds more promises for the design of longer wavelength sensors in the extended short-wave and mid-wave infrared. On the other hand, there are to date only a few reports of imaging based on this material[25,34–37].

As devices based on HgTe NCs demonstrate ever-increasing performance, their stability is becoming a growing concern. The material's inherent stability must be compatible with air operations of the device (possibly after encapsulation) throughout a variety of operating conditions from low to high temperatures (-20 to +50 °C) with the ability to withstand traditional semiconductor processing (baking of resist, exposure to solvents). In the case of CdSe and InP nanocrystals, protecting the material with a Zn-based shell allows long-term operations of the nanocrystals, preserving high PL efficiency above 100 °C, under out-of-equilibrium operations and particularly under large incident photon flux[38]. This improvement has enabled an extension of the display lifetime up to 30 000 hours. In the case of PbS, the surface chemistry has also been optimized to make the material able to sustain post-deposition fabrication, such as pixel etching[39] or deposition of non-reflective coatings[40]. In the case of HgTe NCs, such a study is missing. Here, we aim to identify the strengths and weaknesses of HgTe NCs relevant for optoelectronics.

Our study builds on the recent reporting of photoconductive focal plane array based on HgTe NCs by Greboval *et al*.[25] They report a cost-effective strategy in which a single step of fabrication is required to infrared sensitize a CMOS read-out circuit (ROIC), with an in-plane applied electric field. Since such commercial cameras would require long-term operation, determining the limiting factors for the lifetime of sensors based on HgTe nanocrystals becomes crucial. After fabricating the device, we monitored its performance over time under various operation conditions and while encapsulating it. We then used X-ray photoemission to analyze the robustness of the material to operate in air and found that HgTe nanocrystals are far more stable than PbS nanocrystals that could easily form a PbO shell on their surface. Using thermogravimetric measurements, we then analyze how the temperature affects the film and determine the temperature at which ligands and mercury get removed from the material. Finally, we also study the impact of the particle sintering occurring when the film is exposed to mild annealing. We propose some strategies to overcome this limitation.

Results and discussion

We start by growing nanocrystals of HgTe using the Keuleyan's procedure,[41] during which mercury chloride reacts with trioctylphosphine telluride in oleylamine used as coordinating solvent. The final particle size is driven by the temperature of the reaction (58°C) and the reaction duration (3 min). Eventually, dodecanethiol (Figure S1) is injected to quench the reaction and ensures the particle colloidal stability. The obtained particles present a branched aspect, see **Figure 1**a. This is chosen so that the band edge is close to that of InGaAs, which is traditionally used for short-wave infrared sensing. The absorption band edge appears at around 1.8 µm, while the material is luminescent and presents a PL peak at 2 µm, see **Figure 1**b. To render the material photoconductive, the native ligands are then replaced by shorter ones made of a mixture of $HgCl_2$ and mercaptoethanol[42,43]. The latter procedure leads to a redshift of the band-edge, see **Figure 1**c, and the new cut-off wavelength reaches 2 µm. In the mid-infrared, the relative weight of the C-H bond peak is reduced (Figure S2), which is consistent with a reduction of the ligand length, and a broad peak at 3 µm is the signature of the O-H bond coming from the mercaptoethanol.

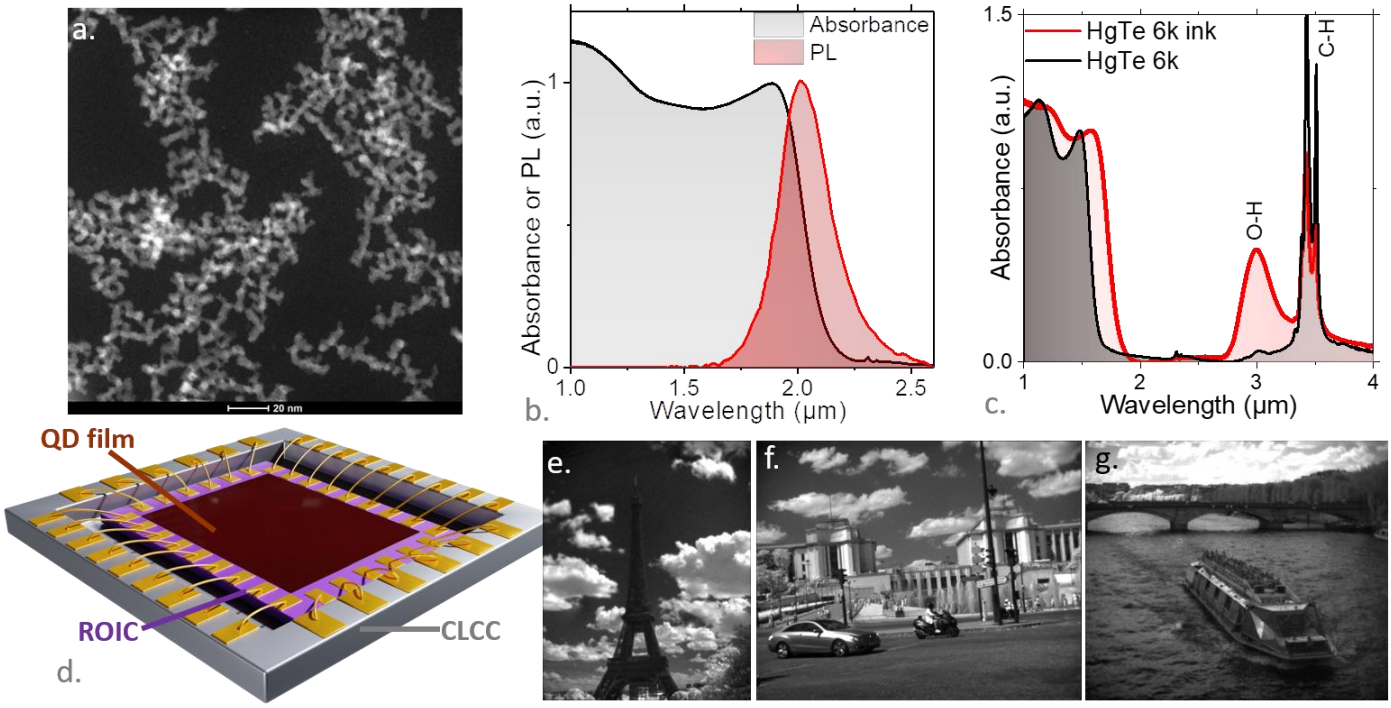

Figure 1 HgTe nanocrystals used for photoconductive focal plane array*. a. STEM-HAADF image of the extended short wave infrared NCs. b. Absorption and photoluminescence spectra of the HgTe NCs. c. Absorption spectra of the HgTe NCs at the end of synthesis and once transformed under ink form. d. Schematic of the extended short-wave infrared sensor used as a photoconductive imager. Part d is adapted from ref 25 with permission from Copyright {2022} Royal Chemical Society. e-g Series of view of Paris city acquired with the HgTe NC-based sensor.*

The obtained ink solution is then spin-coated onto a VGA format read-out circuit (ROIC – model 1601-quantum with planarized surface), **Figure 1**d. The aforementioned ROIC is chosen since it enables application of a different bias on consecutive pixels, leading to the formation of an in-plane electric field, while most ROICs are only compatible with a vertically applied electric field. This configuration allows for a photoconductive operation of the film, considerably easing the device fabrication as opposed to the design of a full homogeneous diode stack. However, this strategy comes at the price of halving the image's resolution. For more details on the operation and performances, see ref [25] and Figure S3 for an image of the camera setup. Typical images acquired with the camera are given in **Figure 1**e-g.

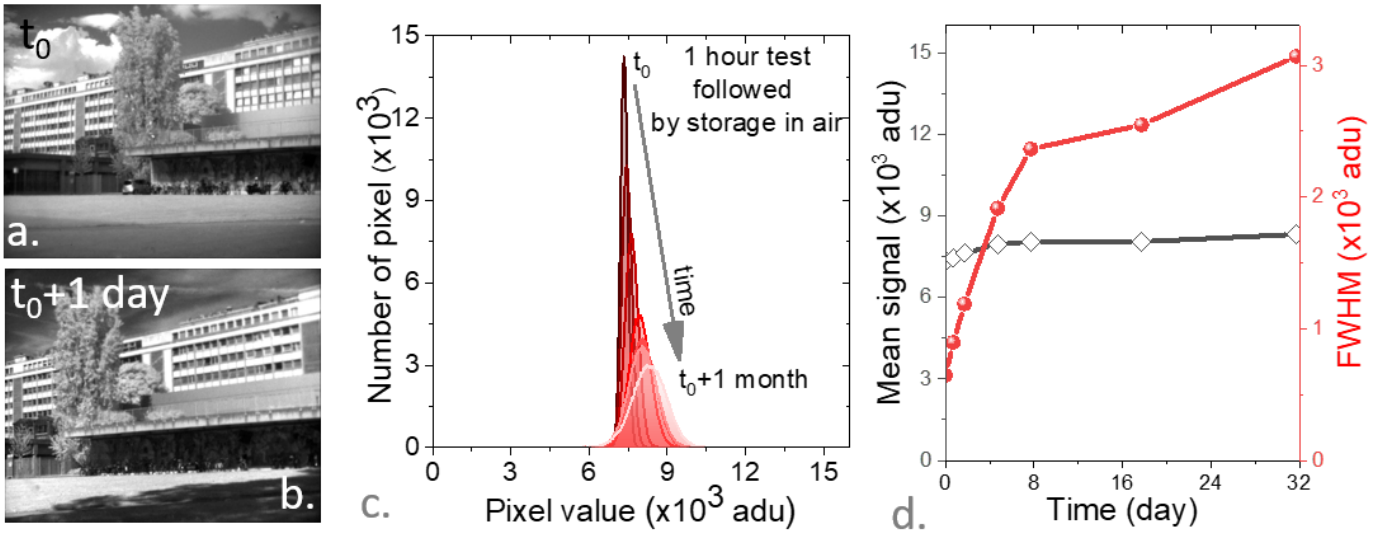

***Figure 2 Aging of the sensor in air**. In this experiment, discrete acquisitions, typically lasting 1h, are operated over one month. During this whole period the sample stays in air. a. (resp. b) image acquired, the first day (resp. the next day, with the same integration time) with the sensor operated without any cooling and in air. c. Histogram of the dark current count, acquired over 50 µs, as a function of time. d. Average full width at half maximum of the dark current histogram quantized in adu (analog digital unit encoded over 14 bits corresponding to 16384 levels), as a function of time.*

We monitored the ROIC's performance for nearly a month while the sensor was operating in air without any thermal management. The image quality is maintained, see **Figure 2**a-b. The histogram of the dark current is presented in **Figure 2**c, and we can only see a slight drift of the dark current over time, though the sensor also becomes less homogeneous, as pointed out by the rise of the histogram linewidth, see **Figure 2**d. To understand what is the origin of this evolution, we have followed the evolution for an encapsulated film of HgTe.[44] In this case, the film is covered by a PMMA and a PVA layer acting respectively as water and oxygen repellant. The same aging trend is observed, see Figure S4. This tends to suggest that the observed aging is not much due to exposure of the ROIC to air or moisture
see Figure S4.

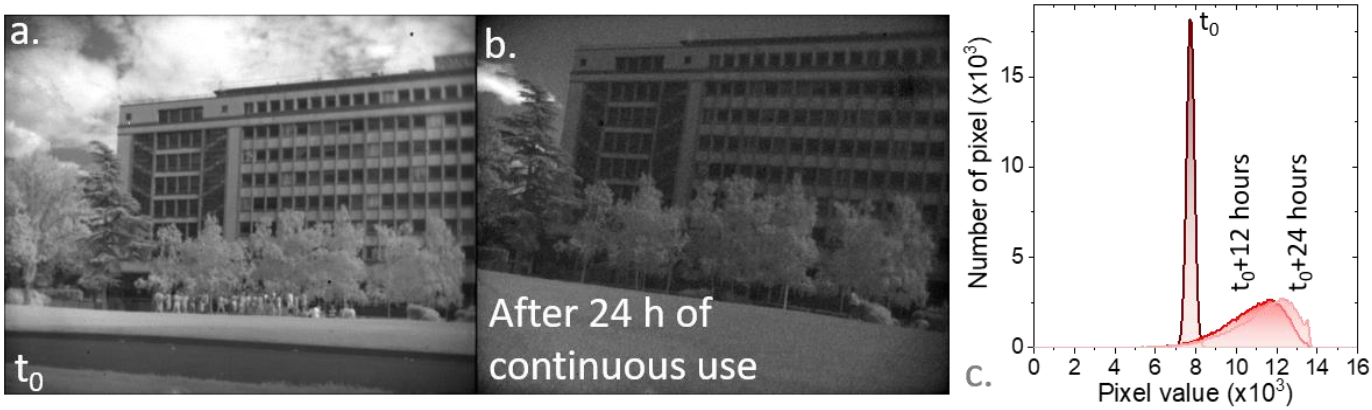

***Figure 3 Aging of the sensor under continuous operation**. In this experiment, the sensor is continuously operated for over one day in air. a. (resp b) image acquired, the first day with 100 µs integration time (resp the next day, with 40 µs integration time) with sensor operated without any cooling and in air. c. Histogram of the dark current count, acquired over 50 µs, as a function of time.*

While we observe minor damage as the device is punctually used and stored in air, we observe a stronger drop in the performance when the camera is continuously operated, see **Figure 3**a-b. After 1 day image gets more granulated and integration time has to be reduced from 100 µs to 40 µs due to the increase of dark current. After only 24h, the dark current has doubled (**Figure 3**c), and the

inhomogeneity (linewidth of the histogram) has increased dramatically. We also observe that in this condition, the film, due to Joule effect in the ROIC, is exposed to relatively high temperatures (see Figure S5). Therefore, in the remainder of the paper, we have used XPS to determine if HgTe gets oxidized and how temperature affects the structural properties of the film.

We used X-ray photoemission (XPS) as a surface-sensitive method to further investigate the HgTe NC surface chemistry. To avoid any charging effects (*i.e.,* a binding energy shift due to the accumulation of holes in the sample after the collection of photoelectrons in the analyzer), samples are systematically processed with short ligands to make them conductive, similar to the way they are made photoconductive. It enables electron reinjection from the substrate after the emission of the photoelectrons. We first use a conventional laboratory instrument to conduct these measurements. The survey spectrum, see **Figure 4**a, confirms the presence of Hg and Te contributions from the inorganic core and S and C from the capping ligands. It also reveals a first striking feature. Despite being prepared in air (*i.e.,* NCs washed in air and the films prepared in air) without any surface cleaning procedures (*i.e.,* films are only degassed under ultrahigh vacuum to conduct the XPS measurements, without further annealing or sputtering), nearly no contribution of oxygen is observed (the expected binding energy for O 1s state is 532 eV). This result contrasts with what has been observed for PbS NCs, which easily get oxidized,[45] leading to a blue shift of the band edge and consequently to the formation of a PbO shell around the PbS particles.

The resolved Te core level spectrum displays a single contribution (**Figure 4**b for Te 4d and Figure S6 for the Te 3d), excluding its oxidation as well.[46,47] The structure of the S 2p states appears more complex with at least three contributions, see **Figure 4**d. There are two contributions on low binding energies (162.3 and 163.8 eV, respectively), compatible with sulfide and thiol forms of sulfur. This suggests that there might be a distribution of ligand coupling with Hg, where strongly bound ligands may appear as sulfides while weakly coupled or free ligands preserve their thiol oxidation state. On top of that, the S 2p states present a third contribution with a binding energy (169.3 eV) consistent with the one expected for oxidized sulfurs. This indicates that some sulfur atoms may be under sulfate form in the NC film. Kamath *et a*l.[48] recently proposed to avoid such oxidized species by conducting the reaction in the dark since the oxidation process of the thiols may be photo-assisted.

Since II-VI semiconductor NCs are generally cation rich on their surface,[49] it is of utmost interest to conduct an XPS analysis of the cations while using more surface-sensitive conditions. This can be obtained by reducing the incident photon energy, which can be done through tunability over a wide energy range accessible with a synchrotron. In this case, the Hg 4f states (acquired with a photon energy of 1253 eV) display two contributions, see **Figure 4**c. The main one appears at a binding energy of 100.3 eV and can be attributed to Hg surrounded by Te atoms in this material. The second contribution appears with a binding energy of 101 eV, and its relative weight is larger as one uses a lower photon energy, see Figure S7. This suggests that this contribution is a surface one. The presence of Hg surface atoms connected to a second population matches with an Hg rich surface where atoms are bound to ligands. Furthermore, because S atoms from the thiolates have a higher electronegativity than Te, those Hg are less electron-rich, explaining why this contribution appears at a higher binding energy.

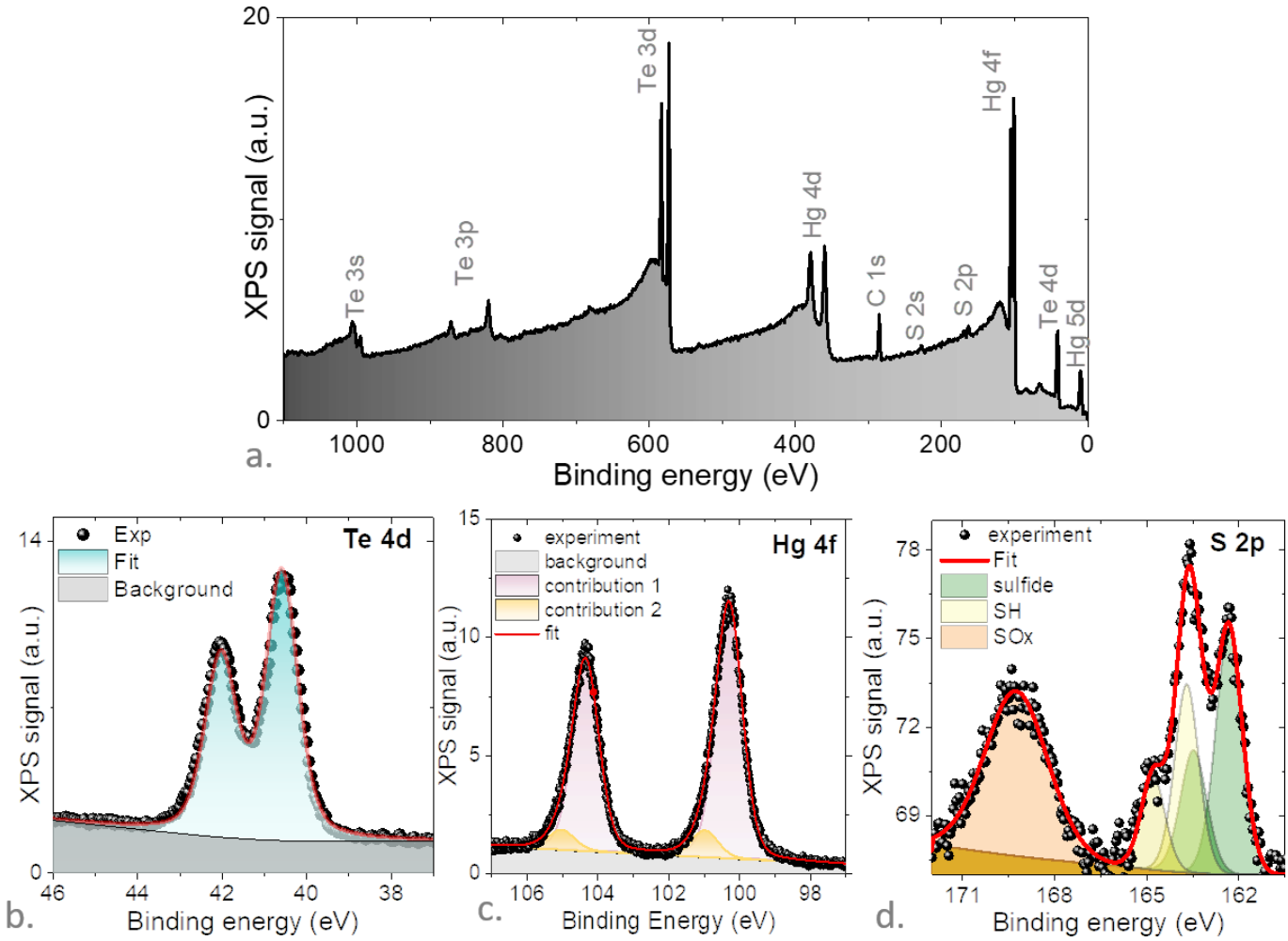

Figure 4 Surface chemistry probed by X-ray photoemission spectroscopy. *a. XPS survey spectrum acquired using an Al Kα line as source (hv=1486 eV) for a HgTe NCs film capped with EDT. b. Te 4d core levels for the same sample (hv=1486 eV). c. Hg 4f core levels for the same sample (acquired with a hv = 1253 eV), also see Figure S7. d. S 2p core levels for the same sample (hv=1486 eV).*

Up to now, we have demonstrated that HgTe NCs appear fairly robust toward oxidation. Nevertheless, this phenomenon can still happen but will mostly occur at the ligand level leading to weaker surface passivation when thiols get oxidized into sulfates. Another relevant parameter to study regarding further integration in optoelectronics is the temperature and, particularly, we would like to determine the temperature range in which the material integrity is preserved. To answer this question, we performed TGA, see **Figure 5**. Starting from room temperature, the temperature is increased, resulting in weight loss, see **Figure 5**a. The first weight loss, around 100 °C, corresponds to solvent (toluene or DMF, depending on surface chemistry) evaporation. We then observe a second weight loss at around 260 °C that matches with the evaporation observed in the case of Hg thiolates only without being observed in the case of bulk HgTe. We can thus attribute it to the evaporation of the ligand shell. Finally, the last weight loss occurs in the 350-400 °C range, which is also observed in the case of bulk HgTe and can be attributed to the melting of the material followed by Hg evaporation.

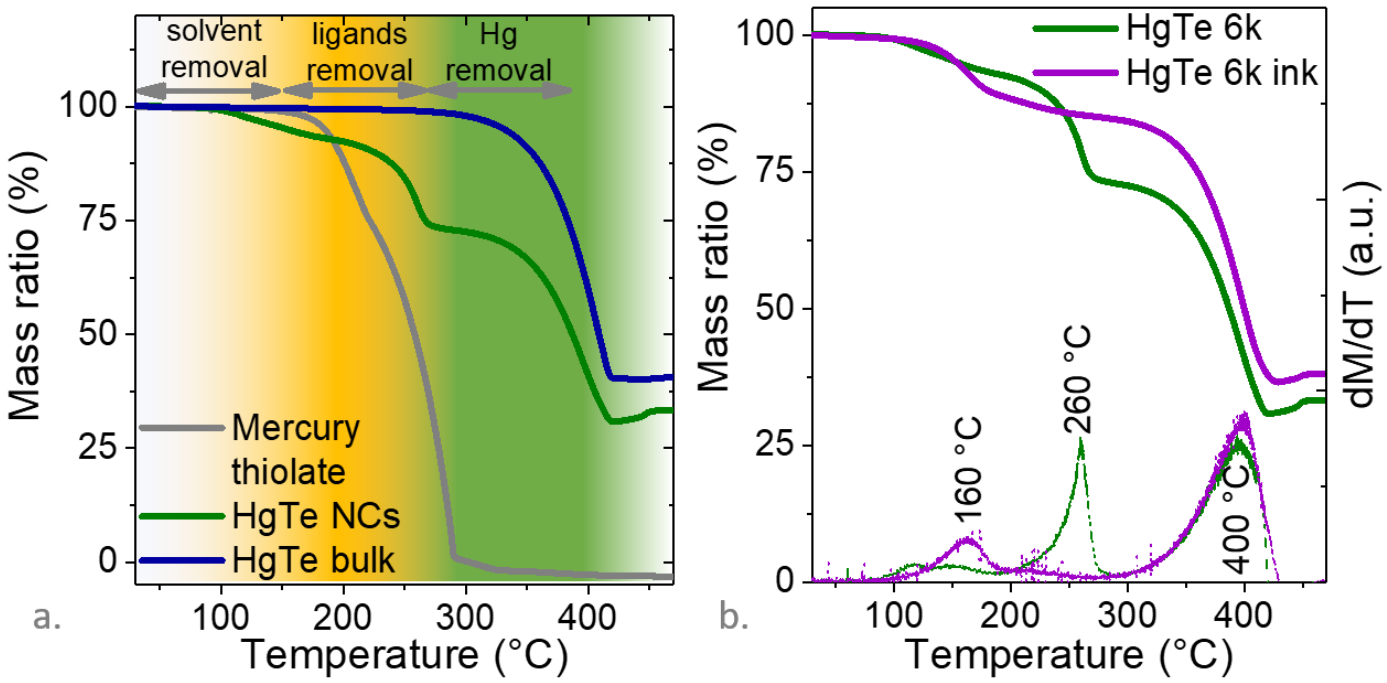

Figure 5* Thermogravimetric analysis *of HgTe NCs. *a. Mass ratio as a function of the temperature for mercury thiolate, HgTe 6k NCs and bulk HgTe. b. Mass ratio as a function of the temperature for HgTe 6k NCs with DDT and under an ink form. The curves at the bottom are the derivative curves to better highlight when the weight loss occurs.*

Though particle sintering already occurs at lower temperatures, as discussed below, this ligand removal sets an upper bound for film processing. In the case of long ligands, the high boiling point of the long alkyl chain (275 °C for dodecanethiol) enables processing at 200 °C while preserving the ligand shell, that is, for example, compatible with atomic layer deposition processes. On the other hand, when the film is processed with shorter ligands, as it is the case in ink-based films, the ligands are removed at a much lower temperature (boiling point of mercaptoethanol at 157 °C), see **Figure 5**b, and the surface chemistry is lost as early as 160 °C.

Though the composition of the photoconductive HgTe NC thin film remains stable up to 160 °C, sintering of the particle can already occur under milder annealing conditions. We followed the absorption spectrum of HgTe films annealed at 50, 75, and 100 °C over time. This temperature range corresponds to the operating temperature of the ROIC, measured to be 57 °C after 15 min of continuous operation, see Figure S5. Note that this exact temperature depends on the operating conditions of the ROIC, and temperatures as high as 80 °C have been measured. While at 50 °C, the spectrum remains unaffected (see Figure S8), at 75 and 100 °C (**Figure 6**a and S8), we observe a large redshift of the spectrum, see **Figure 6**b. This redshift is the signature of a partial loss of quantum confinement induced by the sintering. Greboval *et al.* have[1] provided a sizing curve to link the band edge wavelength λ (in µm) to the equivalent spherical particle size d (in nm): $\lambda=0.17.d^{1.49}$. The measured shift corresponds to an increase of the size from 4.7 nm before annealing to 5.2 nm after 15 min at 75 °C and 6 nm for the same annealing but conducted at 100 °C. Direct measurements of the structural change of the film can be obtained by following the narrowing of the diffraction peak as the film is annealed. The Scherrer size ($L=\lambda_{XRD}. / (FWHM.\cos\theta)$ with $\lambda_{XRD}=0.154$ nm the wavelength of the X-ray line, FWHM the full-width at half maximum of the diffraction peak and θ the diffracted angle) extracted here from the (220) plane direction of the X-ray diffraction pattern, see **Figure 6**c and S9, shows an increase from 4 nm to above 6 nm for annealing at 100 °C.

Aside from the evident shift of the spectral response, this will result in a dramatic increase in the dark current of nanocrystal-based sensors due to its exponential dependence on the band gap. In Figure S10 and **Figure 6**d, we follow the current while the film is annealed in the same conditions as the absorption measurements. Dark current is unaffected by mild annealing at 50 °C and increases only by about a factor 3 after 15 min at 75 °C. On the other hand, at 100 °C, the rise of the dark current becomes dramatic and reaches a factor of 100.

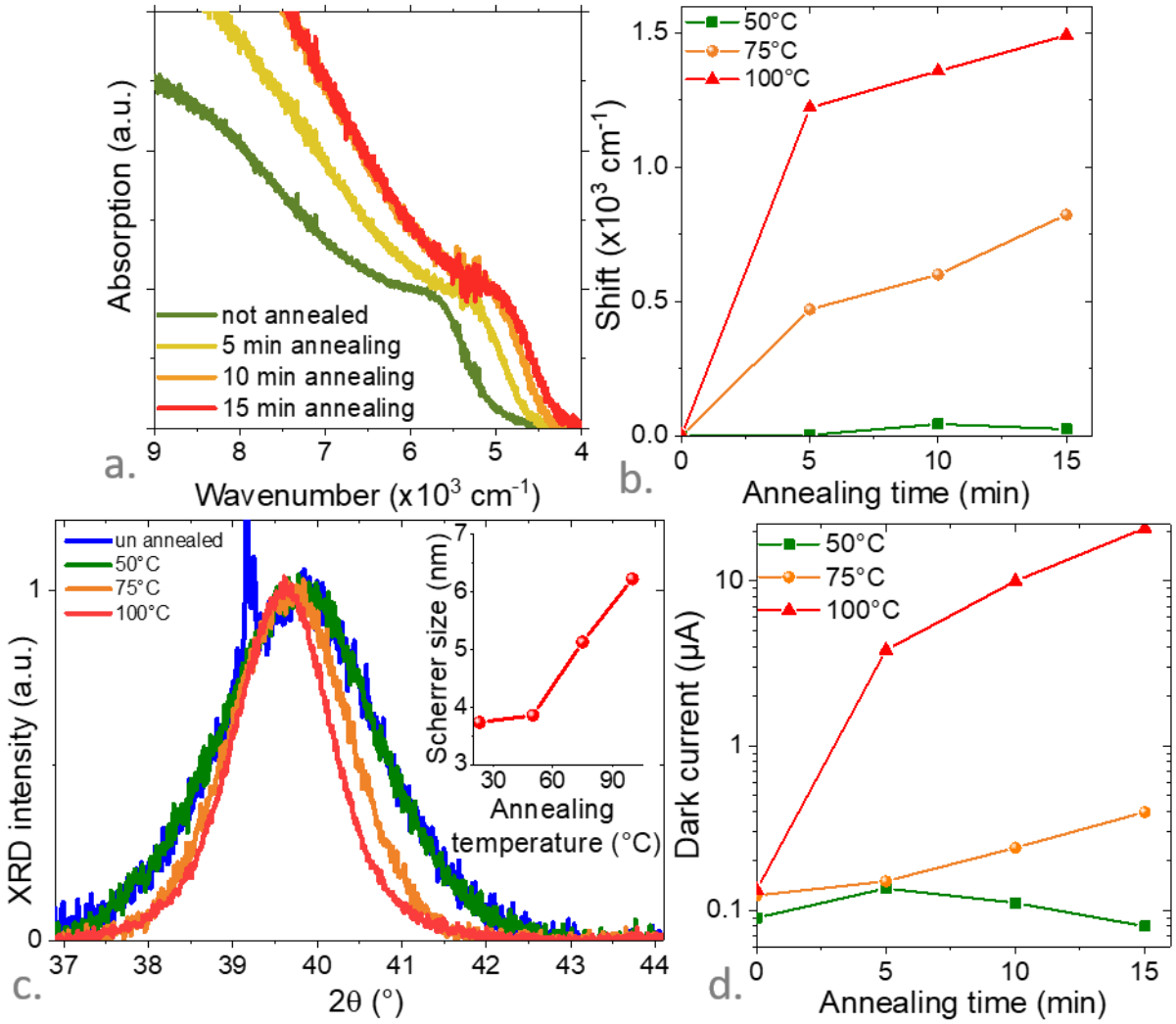

Figure 6 Effect of temperature on structural and optoelectronic properties of the HgTe NC film*. a. Absorption spectra of a HgTe nanocrystal film annealed at 75 °C for various durations. Also see Figure S8 for annealing at 50 and 100 °C. b. Induced spectral shift of the band edge transition resulting from annealing at various temperatures as a function of the annealing duration. c. X-ray diffraction pattern around the (220) peak of the zinc blende phase of HgTe for HgTe NC films annealed at various temperatures. The inset shows the extracted Scherrer size for the HgTe crystallites as a function of the annealing temperature. d. Dark current within an HgTe NC film deposited on interdigitated electrodes and operated under 100 mV as a function of the annealing time at various temperatures. See Figure S9 for IV curves.*

This result stresses the need for a temperature control in such camera. The latter will have a dual role: (i) control the dark current magnitude (reversible change) and (ii) to avoid particle sintering (irreversible change). In Figure S11, we have verified that once coupled to a Peltier stage, enabling temperature control in the -35°C to +30°C range, the dark current histogram stays un affected over time, while it dramatically shifts and broaden when Joule heating is not counter balanced.

Alternatively passive strategies that ensure a higher thermal stability of the material may be considered. Atomic layer deposition (ALD) that infill the inter nanocrystal medium may be used as a possible strategy to prevent particle sintering[50–52], however the implementation of ALD may not

be straightforward since ALD is generally conducted under mild temperature (*ie* generally above the one leading to HgTe NC sintering) and early attempt of low temperature ALD on HgTe NC thin film has led to a loss of photoconductivity[53].

CONCLUSION

To summarize, we have investigated the performance stability of the HgTe NC-based focal plane arrays. Storage in air only leads to a slight drift of the dark current which can be addressed by conducting a two-point correction (dark and gain) of the image. This result is in line with the photoemission data showing that neither Hg nor Te gets oxidized by regular air exposure. Nevertheless, we notice that the ligands are the most prone to oxidation in the film and that oxidized sulfur are easily formed, which likely affects surface passivation. However, it appears that encapsulation is not the most crucial point to consider in order to improve the device stability. In addition, TGA measurement reveals a two-step process: first, a stripping off the ligands above 250 °C, then a mercury evaporation above 350 °C. This is relatively good news since none of these temperatures should be reached typical ROIC operation; thus, we can exclude user Hg vapor exposure. We observe that the primary source of performance drop in our system is the sintering of the particle. The latter starts to be problematic at temperatures ranging from 50 to 75 °C, which is probably high enough for the device to sustain passive storage. On the other hand, in the absence of thermal management strategies, the Joule effect resulting from the current passing in the ROIC can actually bring the device to temperatures where sintering occurs. Given the fact that the material seems to be able to sustain storage up to 50 °C, a simple solution will be the addition of a Peltier cooling stage. More than the reduction of the dark current, the purpose of the cooling stage would be first to prevent the particle sintering resulting from the Joule effect as the ROIC is operated. A long-term goal will be a modification of the material, probably through shelling[48,54], to prevent particle sintering. This objective remains challenging since mercury chalcogenide particles are incompatible with the high-temperature growth required by most shell growth methods.

Experimental section

Chemicals: Mercury chloride ($HgCl_2$, Strem Chemicals, 99%), mercury acetate ($Hg(OAc)_2$, Alfa Aesar, >98%), **Mercury compounds are highly toxic. Handle them with special care.** Tellurium powder (Te, Sigma-Aldrich, 99.99%), trioctylphosphine (TOP) (Alfa, 90%), oleylamine (OLA, Acros, 80-90%), dodecanethiol (DDT, Sigma-Aldrich, 98%), ethanol absolute (VWR), hexane (VWR, 99%), toluene (VWR, 99.5%), chlorobenzene (VWR), methanol (VWR, >98%), N,N dimethylformamide (DMF, VWR), 2-mercaptoethanol (MPOH, Merck, >99%). All chemicals are used without further purification, except oleylamine that is centrifuged before use.

1 M TOP:Te precursor: 6.35 g of Te powder are mixed with 50 mL of TOP in a three-neck flask. The flask is kept under vacuum at room temperature for 5 min before the temperature is raised to 100 °C. Degassing is conducted at this temperature for 20 min. Then, the atmosphere is switched to N_2 and the temperature is raised to 275 °C. The solution is stirred until a clear orange coloration is obtained. The flask is afterwards cooled down to room temperature and the color turns to yellow. Finally, this solution is transferred to a nitrogen-filled glove box for storage.

Mercury thiolate: 3.18 g of mercury acetate are dissolved in 150 mL of water. The mercury solution is then added to a solution of 5 mL of dodecanethiol in 250 mL of ethanol. Mercury dodecylthiolate is precipitated immediately as a white powder. After decantation, the solid product is filtered and

washed several times with ethanol (150 mL). The white powder is dried and recrystallized in hot toluene.

HgTe 6k nanocrystals: In a 100 mL three neck flask, 540 mg of $HgCl_2$ (2 mmol) and 50 mL of oleylamine are degassed under vacuum at 110 °C for 1h. Then, the atmosphere is switched to N_2 and the temperature stabilized at 58 °C. Meanwhile, 2 mL of TOP:Te (1 M) are extracted from the glove box and mixed with 8 mL of oleylamine. Then, the TOP:Te solution is quickly injected. After 3 min, 10 mL of a mixture of 10% DDT in toluene are injected and a water bath is used to quickly decrease the temperature. The content of the flask is split over 4 centrifuge tubes and MeOH is added and the solution is sonicated (3 min). After centrifugation the formed pellets are redispersed in one centrifuge tube with toluene. The solution is precipitated a second time with absolute EtOH and sonicated (3 min). Again, the formed pellet is redispersed in toluene. Then, the nanocrystals are centrifuged in pure toluene to get rid of the lamellar phase. The solid phase is discarded. The stable phase is transferred in a vial after filtration (0.22 µm pore size). The optical density of the NC solution is measured to be ≈1.5 at 400 nm after a 500x dilution, which roughly correspond to 50 $mg.mL^{-1}$.

HgTe ink preparation: We dissolve 30 mg of $HgCl_2$ in a solution of 18 mL of DMF and 2 mL of mercaptoethanol. At each step the solution is stirred with a vortex and an ultrasonic bath. 900 µL of HgTe nanocrystal solution (same concentration as described above) are mixed with 1 mL of the exchange solution. Finally, toluene is added up to reach a global volume of 4 mL and the solution is centrifugated for 2 min at 6000 rpm to precipitate the nanoparticles. The supernatant is discarded and the formed pellet is dried using nitrogen flux and then redispersed in 175 µL of DMF in order to target a thickness of about 100 nm. The obtained solution is called ink. Before ink deposition, the substrate is placed in an oxygen plasma cleaner for 10 min to increase the wettability. The ink is spin-coated on the substrate at 4000 rpm (at 2000 $rpm.s^{-1}$ acceleration) for 30 s. This gives a homogeneous film between 100 nm and 200 nm.

Infrared Absorption spectroscopy: For infrared spectroscopy, we use a Fischer Nicolet iS50 in attenuated total reflection (ATR) mode. The spectra are averaged over 32 acquisitions and have a 4 cm^{-1} resolution.

TEM: A drop of diluted NCs solution is drop-casted onto a copper grid covered with an amorphous carbon film. The grid is degassed overnight under secondary vacuum. Imaging is conducted using a JEOL 2010 transmission electron microscope operated at 200 kV.

X-ray diffraction (XRD) signals of thin films of nanoparticles drop-cast on a silicon substrate are recorded on a Phillips X'Pert diffractometer with a Cu-K**α** radiation. Measurements are performed at a working condition of 40 kV in voltage and 40 mA in current.

(Scanning)-Transmission Electron Microscopy ((S)-TEM) Characterization. Electron microscopy characterization is performed with a FEI Talos transmission electron microscope operating at 200 kV acceleration voltage. These characterizations include bright-field High-Resolution TEM (HRTEM), STEM (probe semi-convergence angle of 10.5 mrad).

X-ray photoemission measurements: Photoemission spectra are collected on an Omicron Argus X-ray photoelectron spectrometer, using a monochromated Al K_α (hv=1486.6eV) radiation source having a 300 W electron beam power. The emission of photoelectrons from the analyzed sample is taken at a takeoff angle of 45° under ultrahigh vacuum (10^{-8} Pa). The spectra are collected with a 20 eV pass energy.

X-ray photoemission measurements on synchrotron*:* For photoemission spectroscopy, we use the Tempo beamline of synchrotron Soleil. Films of nanocrystals are spin-casted onto a gold coated Si substrate (the gold layer was 80 nm thick). The ligands of the nanocrystals are exchanged using the same procedure as for device fabrication to avoid any charging effects during measurements. Samples are introduced in the preparation chamber and degassed until a vacuum below 10^{-9} mbar is reached. Then samples are introduced in the analysis chamber. The signal is acquired by a MBS A-1 photoelectron analyzer equipped with a delay line detector developed by Elettra.[43,55] The acquisition is done at a constant pass energy (50 eV) within the detector. Various photon energies from 150 to 1250 eV are used for the analysis of the core levels. A gold substrate is used to calibrate the Fermi energy. The absolute value of the incoming photon energy is determined by measuring the first and second orders of Au4f core level peaks. Then for a given analyzer pass energy, we measure the Fermi edge and set its binding energy as zero. The same shift is applied to all spectra acquired with the same pass energy. For the deconvolution of the XPS spectra, a linear background was subtracted and Voight function with 20% weighted Lorentzian contribution was used.

Thermogravimetric analysis (TGA): The TGA measurements are carried out on a TA Instruments SDTQ600. Solid samples are obtained as follows: 0.5 mL of the HgTe dispersion in toluene are precipitated by adding methanol, centrifuged and then dried under vacuum overnight. Between 5 and 15 mg of powder are used for each TGA measurement in a platinum crucible. Measurements are performed from 20 °C to 500 °C, with a heating rate of 5 °C/min under a flow of nitrogen.

Focal plane array fabrication: A ROIC packaged in a CLCC is cleaned in a O_2 plasma cleaner for 10 min. The ROIC is then placed on a spincoater and 30 µL of HgTe ink is spincoated at 1000 rpm and an acceleration of 500 rpm.s^{-1} for 60 s and a drying step at 2000 rpm (1000 rpm.s^{-1}) for 120 s. The film is further dried for 2 hours under primary vacuum.

ASSOCIATED CONTENT

Supplementary material includes extra material discussing (*i*) surface chemistry probed by infrared spectroscopy, (*ii*) the focal plane array and its aging, (*iii*) XPS analysis of the HgTe NC film, (*iv*) effect of the sample annealing, (*v*) operation of the sensor with T control.

COMPETING INTEREST

The authors declare no competing financial interests.

ACKNOWLEDGEMENTS

The authors would like to thank Severine Renaudineau from IPCM, Sorbonne Université, for assistance with TGA measurements. The project is supported by ERC starting grants Ne2DeM (grant n° 853049) and blackQD (grant n° 756225). We acknowledge the use of clean-room facilities at the “Centrale de Proximité Paris-Centre”. This work has been supported by Region Ile-de-France in the framework of DIM Nano-K (grant dopQD). This work was supported by French state funds managed by the ANR within the Investissements d'Avenir programme under reference ANR-11-IDEX-0004-02 and, more specifically, within the framework of the Cluster of Excellence MATISSE and by grants IPER-Nano2 (ANR-18CE30-0023-01), Copin (ANR-19-CE24-0022), Frontal (ANR-19-CE09-0017), Graskop (ANR-19-CE09-0026), NITQuantum (ANR-20-ASTR-0008-01), Bright (ANR-21-CE24-0012-02), MixDferro (ANR-21-CE09-0029) and Quickterra (ANR-22-CE09). H.Z. thanks Chinese Scholarship Council for Ph.D. funding.

REFERENCES

(1) Gréboval, C.; Chu, A.; Goubet, N.; Livache, C.; Ithurria, S.; Lhuillier, E. Mercury Chalcogenide Quantum Dots: Material Perspective for Device Integration. *Chem. Rev.* **2021**, *121*, 3627–3700.

(2) Kershaw, S. V.; Rogach, A. L. Infrared Emitting HgTe Quantum Dots and Their Waveguide and Optoelectronic Devices. *Z. Für Phys. Chem.* **2015**, *229*, 23–64.

(3) Green, M.; Mirzai, H. Synthetic Routes to Mercury Chalcogenide Quantum Dots. *J. Mater. Chem. C* **2018**, *6*, 5097–5112.

(4) Kershaw, S. V.; Yiu, W. K.; Sergeev, A.; Rogach, A. L. Development of Synthetic Methods to Grow Long-Wavelength Infrared-Emitting HgTe Quantum Dots in Dimethylformamide. *Chem. Mater.* **2020**, *32*, 3930–3943.

(5) Rogach, A.; Kershaw, S. V.; Burt, M.; Harrison, M. T.; Kornowski, A.; Eychmüller, A.; Weller, H. Colloidally Prepared HgTe Nanocrystals with Strong Room-Temperature Infrared Luminescence. *Adv. Mater.* **1999**, *11*, 552–555.

(6) Kershaw, S. V.; Harrison, M.; Rogach, A. L.; Kornowski, A. Development of IR-Emitting Colloidal II-VI Quantum-Dot Materials. *IEEE J. Sel. Top. Quantum Electron.* **2000**, *6*, 534–543.

(7) Goubet, N.; Jagtap, A.; Livache, C.; Martinez, B.; Portalès, H.; Xu, X. Z.; Lobo, R. P. S. M.; Dubertret, B.; Lhuillier, E. Terahertz HgTe Nanocrystals: Beyond Confinement. *J. Am. Chem. Soc.* **2018**, *140*, 5033–5036.

(8) Shen, X.; Peterson, J. C.; Guyot-Sionnest, P. Mid-Infrared HgTe Colloidal Quantum Dot LEDs. *ACS Nano* **2022**, *16*, 7301–7308.

(9) Qu, J.; Rastogi, P.; Gréboval, C.; Lagarde, D.; Chu, A.; Dabard, C.; Khalili, A.; Cruguel, H.; Robert, C.; Xu, X. Z.; Ithurria, S.; Silly, M. G.; Ferré, S.; Marie, X.; Lhuillier, E. Electroluminescence from HgTe Nanocrystals and Its Use for Active Imaging. *Nano Lett.* **2020**, *20*, 6185–6190.

(10) Qu, J.; Weis, M.; Izquierdo, E.; Mizrahi, S. G.; Chu, A.; Dabard, C.; Gréboval, C.; Bossavit, E.; Prado, Y.; Péronne, E.; Ithurria, S.; Patriarche, G.; Silly, M. G.; Vincent, G.; Boschetto, D.; Lhuillier, E. Electroluminescence from Nanocrystals above 2 Mm. *Nat. Photonics* **2022**, *16*, 38–44.

(11) Geiregat, P.; Houtepen, A. J.; Sagar, L. K.; Infante, I.; Zapata, F.; Grigel, V.; Allan, G.; Delerue, C.; Van Thourhout, D.; Hens, Z. Continuous-Wave Infrared Optical Gain and Amplified Spontaneous Emission at Ultralow Threshold by Colloidal HgTe Quantum Dots. *Nat. Mater.* **2018**, *17*, 35–42.

(12) Olk, P.; Buchler, B. C.; Sandoghdar, V.; Gaponik, N.; Eychmüller, A.; Rogach, A. L. Subwavelength Emitters in the Near-Infrared Based on Mercury Telluride Nanocrystals. *Appl. Phys. Lett.* **2004**, *84*, 4732–4734.

(13) Shopova, S. I.; Farca, G.; Rosenberger, A. T.; Wickramanayake, W. M. S.; Kotov, N. A. Microsphere Whispering-Gallery-Mode Laser Using HgTe Quantum Dots. *Appl. Phys. Lett.* **2004**, *85*, 6101–6103.

(14) Dang, T. H.; Vasanelli, A.; Todorov, Y.; Sirtori, C.; Prado, Y.; Chu, A.; Gréboval, C.; Khalili, A.; Cruguel, H.; Delerue, C.; Vincent, G.; Lhuillier, E. Bias Tunable Spectral Response of Nanocrystal Array in a Plasmonic Cavity. *Nano Lett.* **2021**, *21*, 6671–6677.

(15) Tang, X.; Chen, M.; Ackerman, M. M.; Melnychuk, C.; Guyot-Sionnest, P. Direct Imprinting of Quasi-3D Nanophotonic Structures into Colloidal Quantum-Dot Devices. *Adv. Mater.* **2020**, *32*, 1906590.

(16) Chen, M.; Lu, L.; Yu, H.; Li, C.; Zhao, N. Integration of Colloidal Quantum Dots with Photonic Structures for Optoelectronic and Optical Devices. *Adv. Sci.* **2021**, *8*, 2101560.

(17) Chen, M.; Lu, H.; Abdelazim, N. M.; Zhu, Y.; Wang, Z.; Ren, W.; Kershaw, S. V.; Rogach, A. L.; Zhao, N. Mercury Telluride Quantum Dot Based Phototransistor Enabling High-Sensitivity Room-Temperature Photodetection at 2000 Nm. *ACS Nano* **2017**, *11*, 5614–5622.

(18) Dong, Y.; Chen, M.; Yiu, W. K.; Zhu, Q.; Zhou, G.; Kershaw, S. V.; Ke, N.; Wong, C. P.; Rogach, A. L.; Zhao, N. Solution Processed Hybrid Polymer: HgTe Quantum Dot

Phototransistor with High Sensitivity and Fast Infrared Response up to 2400 Nm at Room Temperature. *Adv. Sci.* **2020**, *7*, 2000068.
(19) Zhu, B.; Chen, M.; Zhu, Q.; Zhou, G.; Abdelazim, N. M.; Zhou, W.; Kershaw, S. V.; Rogach, A. L.; Zhao, N.; Tsang, H. K. Integrated Plasmonic Infrared Photodetector Based on Colloidal HgTe Quantum Dots. *Adv. Mater. Technol.* **2019**, *4*, 1900354.
(20) Cryer, M. E.; Halpert, J. E. 300 Nm Spectral Resolution in the Mid-Infrared with Robust, High Responsivity Flexible Colloidal Quantum Dot Devices at Room Temperature. *ACS Photonics* **2018**, *5*, 3009–3015.
(21) Yang, J.; Hu, H.; Lv, Y.; Yuan, M.; Wang, B.; He, Z.; Chen, S.; Wang, Y.; Hu, Z.; Yu, M.; Zhang, X.; He, J.; Zhang, J.; Liu, H.; Hsu, H.-Y.; Tang, J.; Song, H.; Lan, X. Ligand-Engineered HgTe Colloidal Quantum Dot Solids for Infrared Photodetectors. *Nano Lett.* **2022**, *22*, 3465–3472.
(22) Grotevent, M. J.; Hail, C. U.; Yakunin, S.; Dirin, D. N.; Thodkar, K.; Borin Barin, G.; Guyot-Sionnest, P.; Calame, M.; Poulikakos, D.; Kovalenko, M. V.; Shorubalko, I. Nanoprinted Quantum Dot–Graphene Photodetectors. *Adv. Opt. Mater.* **2019**, *7*, 1900019.
(23) Chu, A.; Gréboval, C.; Prado, Y.; Majjad, H.; Delerue, C.; Dayen, J.-F.; Vincent, G.; Lhuillier, E. Infrared Photoconduction at the Diffusion Length Limit in HgTe Nanocrystal Arrays. *Nat. Commun.* **2021**, *12*, 1794.
(24) Chu, A.; Gréboval, C.; Goubet, N.; Martinez, B.; Livache, C.; Qu, J.; Rastogi, P.; Bresciani, F. A.; Prado, Y.; Suffit, S.; Ithurria, S.; Vincent, G.; Lhuillier, E. Near Unity Absorption in Nanocrystal Based Short Wave Infrared Photodetectors Using Guided Mode Resonators. *ACS Photonics* **2019**, *6*, 2553–2561.
(25) Gréboval, C.; Darson, D.; Parahyba, V.; Alchaar, R.; Abadie, C.; Noguier, V.; Ferré, S.; Izquierdo, E.; Khalili, A.; Prado, Y.; Potet, P.; Lhuillier, E. Photoconductive Focal Plane Array Based on HgTe Quantum Dots for Fast and Cost-Effective Short-Wave Infrared Imaging. *Nanoscale* **2022**, *14*, 9359–9368.
(26) Georgitzikis, E.; Malinowski, P. E.; Li, Y.; Maes, J.; Hagelsieb, L. M.; Guerrieri, S.; Hens, Z.; Heremans, P.; Cheyns, D. Integration of PbS Quantum Dot Photodiodes on Silicon for NIR Imaging. *IEEE Sens. J.* **2020**, *20*, 6841–6848.
(27) SWIR Vision https://www.swirvisionsystems.com (accessed Jan 28, 2022).
(28) Gregory, C.; Hilton, A.; Violette, K.; Klem, E. J. D. 66-3: *Invited Paper:* Colloidal Quantum Dot Photodetectors for Large Format NIR, SWIR, and ESWIR Imaging Arrays. *SID Symp. Dig. Tech. Pap.* **2021**, *52*, 982–986.
(29) Hafiz, S. B.; Scimeca, M.; Sahu, A.; Ko, D.-K. Colloidal Quantum Dots for Thermal Infrared Sensing and Imaging. *Nano Converg.* **2019**, *6*, 7.
(30) Nakotte, T.; Munyan, S. G.; Murphy, J. W.; Hawks, S. A.; Kang, S.; Han, J.; Hiszpanski, A. M. Colloidal Quantum Dot Based Infrared Detectors: Extending to the Mid-Infrared and Moving from the Lab to the Field. *J. Mater. Chem. C* **2022**, *10*, 790–804.
(31) Steckel, J. S.; Josse, E.; Pattantyus-Abraham, A. G.; Bidaud, M.; Mortini, B.; Bilgen, H.; Arnaud, O.; Allegret-Maret, S.; Saguin, F.; Mazet, L.; et al. Global Shutter Quantum Dot Image Sensor Optimized for Near and Shortwave Infrared. In *2021 IEEE International Electron Devices Meeting (IEDM)*; IEEE: San Francisco, CA, USA, 2021; p 23.4.1-23.4.4.
(32) Malinowski, Pawel. Building Low-Cost Infrared Sensors with Sub-Micron Films. *Imaging Mach. Vis. Eur.* **2019**, *93*, 16–18.
(33) Kim, J. H.; Pejovic, V.; Georgitzikis, E.; Li, Y.; Kim, J.; Malinowski, P. E.; Lieberman, I.; Cheyns, D.; Heremans, P.; Lee, J. Detailed Characterization of Short-Wave Infrared Colloidal Quantum Dot Image Sensors. *IEEE Trans. Electron Devices* **2022**, *69*, 2900–2906.
(34) Ciani, A. J.; Pimpinella, R. E.; Grein, C. H.; Guyot-Sionnest, P. Colloidal Quantum Dots for Low-Cost MWIR Imaging. In *Infrared Technology and Applications XLII*; International Society for Optics and Photonics, 2016; Vol. 9819, p 981919.
(35) Buurma, C.; Pimpinella, R. E.; Ciani, A. J.; Feldman, J. S.; Grein, C. H.; Guyot-Sionnest, P. MWIR Imaging with Low Cost Colloidal Quantum Dot Films. In *Optical Sensing, Imaging, and Photon Counting: Nanostructured Devices and Applications 2016*; International Society for Optics and Photonics, 2016; Vol. 9933, p 993303.

(36) Chatterjee, A.; Pendyala, N. B.; Jagtap, A.; Rao, K. S. R. K. Uncooled Mid-Wave Infrared Focal Plane Array Using Band Gap Engineered Mercury Cadmium Telluride Quantum Dot Coated Silicon ROIC. *E-J. Surf. Sci. Nanotechnol.* **2019**, *17*, 95–100.
(37) Chu, A.; Martinez, B.; Ferré, S.; Noguier, V.; Gréboval, C.; Livache, C.; Qu, J.; Prado, Y.; Casaretto, N.; Goubet, N.; Cruguel, H.; Dudy, L.; Silly, M. G.; Vincent, G.; Lhuillier, E. HgTe Nanocrystals for SWIR Detection and Their Integration up to the Focal Plane Array. *ACS Appl. Mater. Interfaces* **2019**, *11*, 33116–33123.
(38) Wang, C.-F.; Fan, F.; Sabatini, R. P.; Voznyy, O.; Bicanic, K.; Li, X.; Sellan, D. P.; Saravanapavanantham, M.; Hossain, N.; Chen, K.; Hoogland, S.; Sargent, E. H. Quantum Dot Color-Converting Solids Operating Efficiently in the KW/Cm ^{2} Regime. *Chem. Mater.* **2017**, *29*, 5104–5112.
(39) Li, Y.; Karve, G.; Malinowski, P. E.; Kim, J. H.; Georgitzikis, E.; Pejovic, V.; Lim, M.-J.; Hagelsieb, L. M.; Puybaret, R.; Lieberman, I.; Lee, J.; Cheyns, D.; Heremans, P.; Osman, H.; Tezcan, D. S. Wafer Level Pixelation of Colloidal Quantum Dot Image Sensors. In *2022 IEEE Symposium on VLSI Technology and Circuits (VLSI Technology and Circuits)*; IEEE: Honolulu, HI, USA, 2022; pp 349–350.
(40) Liu, J.; Liu, P.; Chen, D.; Shi, T.; Qu, X.; Chen, L.; Wu, T.; Ke, J.; Xiong, K.; Li, M.; Song, H.; Wei, W.; Cao, J.; Zhang, J.; Gao, L.; Tang, J. A Near-Infrared Colloidal Quantum Dot Imager with Monolithically Integrated Readout Circuitry. *Nat. Electron.* **2022**, *5*, 443–451.
(41) Keuleyan, S.; Lhuillier, E.; Guyot-Sionnest, P. Synthesis of Colloidal HgTe Quantum Dots for Narrow Mid-IR Emission and Detection. *J. Am. Chem. Soc.* **2011**, *133*, 16422–16424.
(42) Martinez, B.; Ramade, J.; Livache, C.; Goubet, N.; Chu, A.; Gréboval, C.; Qu, J.; Watkins, W. L.; Becerra, L.; Dandeu, E.; Fave, J. L.; Méthivier, C.; Lacaze, E.; Lhuillier, E. HgTe Nanocrystal Inks for Extended Short-Wave Infrared Detection. *Adv. Opt. Mater.* **2019**, *7*, 1900348.
(43) Lan, X.; Chen, M.; Hudson, M. H.; Kamysbayev, V.; Wang, Y.; Guyot-Sionnest, P.; Talapin, D. V. Quantum Dot Solids Showing State-Resolved Band-like Transport. *Nat. Mater.* **2020**, *19*, 323–329.
(44) Jagtap, A.; Goubet, N.; Livache, C.; Chu, A.; Martinez, B.; Gréboval, C.; Qu, J.; Dandeu, E.; Becerra, L.; Witkowski, N.; Ithurria, S.; Mathevet, F.; Silly, M. G.; Dubertret, B.; Lhuillier, E. Short Wave Infrared Devices Based on HgTe Nanocrystals with Air Stable Performances. *J. Phys. Chem. C* **2018**, *122*, 14979–14985.
(45) Zherebetskyy, D.; Scheele, M.; Zhang, Y.; Bronstein, N.; Thompson, C.; Britt, D.; Salmeron, M.; Alivisatos, P.; Wang, L.-W. Hydroxylation of the Surface of PbS Nanocrystals Passivated with Oleic Acid. *Science* **2014**, *344*, 1380–1384.
(46) Tari, S.; Aqariden, F.; Chang, Y.; Grein, C.; Li, J.; Kioussis, N. Impact of Surface Treatment on the Structural and Electronic Properties of Polished CdZnTe Surfaces for Radiation Detectors. *J. Electron. Mater.* **2013**, *42*, 3252–3258.
(47) Reese, M. O.; Perkins, C. L.; Burst, J. M.; Farrell, S.; Barnes, T. M.; Johnston, S. W.; Kuciauskas, D.; Gessert, T. A.; Metzger, W. K. Intrinsic Surface Passivation of CdTe. *J. Appl. Phys.* **2015**, *118*, 155305.
(48) Kamath, A.; Melnychuk, C.; Guyot-Sionnest, P. Toward Bright Mid-Infrared Emitters: Thick-Shell n-Type HgSe/CdS Nanocrystals. *J. Am. Chem. Soc.* **2021**, *143*, 19567–19575.
(49) Houtepen, A. J.; Hens, Z.; Owen, J. S.; Infante, I. On the Origin of Surface Traps in Colloidal II–VI Semiconductor Nanocrystals. *Chem. Mater.* **2017**, *29*, 752–761.
(50) Liu, Y.; Tolentino, J.; Gibbs, M.; Ihly, R.; Perkins, C. L.; Liu, Y.; Crawford, N.; Hemminger, J. C.; Law, M. PbSe Quantum Dot Field-Effect Transistors with Air-Stable Electron Mobilities above 7 Cm ^{2} V $^{-1}$ s $^{-1}$. *Nano Lett.* **2013**, *13*, 1578–1587.
(51) Hu, C.; Gassenq, A.; Justo, Y.; Devloo-Casier, K.; Chen, H.; Detavernier, C.; Hens, Z.; Roelkens, G. Air-Stable Short-Wave Infrared PbS Colloidal Quantum Dot Photoconductors Passivated with Al $_{2}$ O $_{3}$ Atomic Layer Deposition. *Appl. Phys. Lett.* **2014**, *105*, 171110.
(52) Devloo-Casier, K.; Geiregat, P.; Ludwig, K. F.; van Stiphout, K.; Vantomme, A.; Hens, Z.; Detavernier, C.; Dendooven, J. A Case Study of ALD Encapsulation of Quantum Dots: Embedding Supported CdSe/CdS/ZnS Quantum Dots in a ZnO Matrix. *J. Phys. Chem. C* **2016**, *120*, 18039–18045.

(53) Lhuillier, E.; Keuleyan, S.; Guyot-Sionnest, P. Transport Properties of Mid-Infrared Colloidal Quantum Dot Films; Proc. SPIE 8271, Quantum Dots and Nanostructures: Synthesis, Characterization, and Modeling IX, 827109 **2012**; https://doi.org/10.1117/12.906423
(54) Shen, G.; Guyot-Sionnest, P. HgTe/CdTe and HgSe/CdX (X = S, Se, and Te) Core/Shell Mid-Infrared Quantum Dots. *Chem. Mater.* **2019**, *31*, 286–293.
(55) Bergeard, N.; Silly, M. G.; Krizmancic, D.; Chauvet, C.; Guzzo, M.; Ricaud, J. P.; Izquierdo, M.; Stebel, L.; Pittana, P.; Sergo, R.; Cautero, G.; Dufour, G.; Rochet, F.; Sirotti, F. Time-Resolved Photoelectron Spectroscopy Using Synchrotron Radiation Time Structure. *J. Synchrotron Radiat.* **2011**, *18*, 245–250.

Table of content graphic